RSC Advances

PAPER

View Article Online
View Journal | View Issue

Cite this: *RSC Adv.*, 2023, **13**, 33463

A high mass loading flexible electrode with a sheet-like Mn_3O_4/$NiMoO_4$@NiCo LDH on a carbon cloth for supercapacitors†

Ruibin Liang,‡[a] Si Liu,‡[a] Jianrong Lin,[a] Jingfei Dai,[a] Jingyi Peng,[a] Peiyuan Huang,[a] Jianwen Chen [b] and Peng Xiao *[a]

Received 12th October 2023
Accepted 31st October 2023

DOI: 10.1039/d3ra06937k

rsc.li/rsc-advances

Mass loading is an important parameter to evaluate the application potential of active materials in high-capacity supercapacitors. Synthesizing active materials with high mass loading is a promising strategy to improve high performance energy storage devices. Preparing electrode materials with a porous structure is of significance to overcome the disadvantages brought by high mass loading. In this work, a Mn_3O_4/$NiMoO_4$@NiCo layered double hydroxide (MO/NMO/NiCo LDH) positive electrode is fabricated on a carbon cloth with a high mass loading of 20.4 mg cm^{-2}. The MO/NMO/NiCo LDH presents as a special three-dimensional porous nanostructure and exhibits a high specific capacitance of 815 F g^{-1} at 1 A g^{-1}. Impressively, the flexible supercapacitor based on the MO/NMO/NiCo LDH positive electrode and an AC negative electrode delivers a maximum energy density of 22.5 W h kg^{-1} and a power density of 8730 W kg^{-1}. It also retains 60.84% of the original specific capacitance after bending to 180° 600 times. Moreover, it exhibits 76.92% capacitance retention after 15 000 charge/discharge cycles. These results make MO/NMO/NiCo LDH one of the most attractive candidates of positive electrode materials for high-performance flexible supercapacitors.

1 Introduction

In the past decades, supercapacitors (SCs) have been widely considered as potential energy storage equipment because of their high power density, good safety, and long-life cycle.[1,2] However, low energy density remains a bottleneck and developing new electrode materials is an effective approach to attain high energy density for SCs.[3] It is well known that the electrochemical performance of supercapacitors is determined by the electrode materials. At present, it is difficult for a single electrode material to break through the inherent disadvantage barrier of energy storage. In recent years, a lot of attention has been given to designing and synthesizing composite electrode materials owing to the synergistic effect between different components. Barua and co-workers prepared a graphene-MOF aerogel electrode with a low mass loading of 3 mg cm^{-2}, which provided a high specific capacitance of 98 F g^{-1} at 0.5 A g^{-1}.[4] The 3D-porous Ni/MnO_x nanocomposite prepared by Ashassi-Sorkhabi *et al.* had a low mass loading of 1.65 mg cm^{-2} and showed a specific capacitance of 396.4 F g^{-1} at 0.3 A g^{-1}. The composite also showed an excellent stability of 100% after 25 000 cycles.[5]

Nevertheless, the electrochemical performance of the above electrode materials was achieved with a low mass loading. In fact, the mass loading is the key parameter for some electrode materials in practical applications.[6] It is usually necessary to achieve an active material mass loading of 8–10 mg cm^{-2} to build pseudocapacitors for commercial applications.[7] However, due to the poor conductivity of metal oxides, the high mass loading affects the conductivity and ion diffusion of the electrode, thereby seriously reducing the specific capacitance, rate performance, and cycle life of supercapacitors. For example, manganese dioxide (MnO_2) with a thickness of less than 1 μm can exhibit ultra-high specific capacitance. However, the high mass loading of MnO_2 leads to a reduction in specific capacitance due to the close-packed structures causing limited active specific area.[8] Therefore, preparing SCs with high energy density and high mass loading electrodes is full of challenges.[9] Electrode materials with three-dimensional (3D) porous nanostructures can ensure the rapid transport of ions and electrons through the whole electrode and mechanical stability, which provide a guarantee for its good electrochemical performance on high mass loading.

In this work, we prepared high mass loading (20.4 mg cm^{-2}) Mn_3O_4/$NiMoO_4$@NiCo LDH (MO/NMO/NiCo LDH) on carbon cloth (CC) by electrodeposition followed by a two-step

[a]Guangdong-Hong Kong-Macao Joint Laboratory for Intelligent Micro-Nano Optoelectronic Technology, School of Physics and Optoelectronic Engineering, Foshan University, Foshan 528225, China. E-mail: xiaopeng@fosu.edu.cn

[b]School of Electronic and Information Engineering, Foshan University, Foshan, 528000, China

† Electronic supplementary information (ESI) available. See DOI: https://doi.org/10.1039/d3ra06937k

‡ These authors contributed equally to this work.

hydrothermal method. Sheet-like MO/NMO/NiCo LDH exhibited a 3D porous nanostructure. The MO/NMO/NiCo LDH electrode delivered 815 F g^{-1} at 1 A g^{-1}. The MO/NMO/NiCo LDH// active carbon (AC) flexible supercapacitor (FSC) showed great potential in actual application. It exhibited an energy density of 22.5 W h kg^{-1} at 997.53 W kg^{-1}. Even when the power density reached 8730 W kg^{-1}, 1.944 W h kg^{-1} of energy density was retained. Importantly, the FSC keeps 60.84% of its original specific capacitance after bending to 180° 600 times. It also kept 184.62% of the original specific capacitance after 8000 charge/discharge cycles and eventually retained 76.92% after 15 000 cycles. The MO/NMO/NiCo LDH electrode showed potential for use in a high-performance SC with a high mass loading electrode.

2 Discussion

Fig. 1a shows the X-ray diffraction (XRD) pattern of MO/NMO/NiCo LDH. The diffraction peaks at 41.764°, 43.936°, 47.384°, 53.175° and 61.946° belong to the (100), (004), (102), (103) and (104) planes of CC (PDF#26-1078). The distraction peaks at 17.196°, 28.735°, 31.356°, 44.148° and 59.477° correspond to the (101), (112), (200), (220) and (224) planes of Mn_3O_4 (PDF#16-0154). The distraction peaks at 13.491°, 26.308°, 43.936°, 47.384°, 53.175°, 57.859, 61.946 and 63.093° accord with $NiMoO_4$ (PDF#18-0879). The peaks at 17.196° (020), 20.049° (001), 26.819° (220), 33.674° (221), 35.036° (040), 36.399° (301), 39.507° (231) and 47.384° (340) match to NiCo LDH (PDF#48-0083). Fig. 1b and c show that massive sheet-like MO/NMO/NiCo LDH coats the surface of the CC to construct a porous structure, favoring contact between the active material and the electrolyte. This provides not only numerous ion/electron transport channels for redox reaction processing, but also ample space for material expansion/contraction, which helps maintain high specific capacitance with high mass loading and ensures good cycle stability during long charge/discharge processes. The element mapping corresponding to the scanning electron microscopy (SEM) image is shown in Fig. 1d–h and the co-existence of Ni, Co, Mo and Mn was confirmed.

The X-ray photoelectron spectroscopy (XPS) spectrum of MO/NMO/NiCo LDH is shown in Fig. S1† and includes Ni, Co, Mn, Mo, O and C. As shown in Fig. 2a, there are two major peaks and two satellite peaks in the Ni 2p XPS spectrum.[10] The peaks at 855.46 eV and 857.26 eV accord with Ni $2p_{3/2}$. The peaks at 872.95 eV and 874.77 eV originate from Ni $2p_{1/2}$. The peaks at 861.39 eV (Ni $2p_{3/2}$ sat.) and 879.58 eV (Ni $2p_{1/2}$ sat.) are satellite peaks. This proves the existence of Ni^{2+}.[11] Fig. 2b shows that the Co $2p_{3/2}$ peaks (780.61 eV and 783.37 eV) and Co $2p_{1/2}$ peaks (796.59 eV and 798.79 eV) contribute to the major peaks of the Co 2p spectrum and the peaks at 786.94 eV and 802.66 eV correspond to the satellite peaks. The existence of Co^{2+} is further confirmed by the binding energy difference between the peaks of Co $2p_{3/2}$ (781.03 eV) and Co $2p_{1/2}$ (797.01 eV), which is near 16.00 eV. As shown in the Mo 3d spectrum (Fig. 2c), the existence of Mo^{6+} is revealed by the peaks at 232.10 eV (Mo $3d_{5/2}$) and 235.17 eV (Mo $3d_{3/2}$).[12] Fig. 2d shows the XPS spectrum of Mn 2p. The peaks at 638.05 eV (Mn^{2+} $2p_{3/2}$), 643.89 eV (Mn^{2+} $2p_{3/2}$) and 650.89 eV (Mn^{2+} $2p_{1/2}$) are from Mn^{2+}. The peak at 646.83 eV corresponds to Mn $2p_{3/2}$. The binding energy difference between 641.26 eV and 653.05 eV is 11.79 eV, which proves the existence of Mn_3O_4.

Fig. 3a shows the cyclic voltammetry (CV) curves of each sample at the scan rate of 30 mV s^{-1}. All the CV curves show redox peaks, which means that energy is stored by redox reaction.[13] In addition, the CV area of MO/NMO/NiCo LDH is obviously larger than those of MO/NMO and MO/NiCo LDH, indicating that MO/NMO/NiCo LDH has better capacitance performance than the other samples. Fig. 3b shows the galvanostatic charge/discharge (GCD) curves at 1 A g^{-1} of the

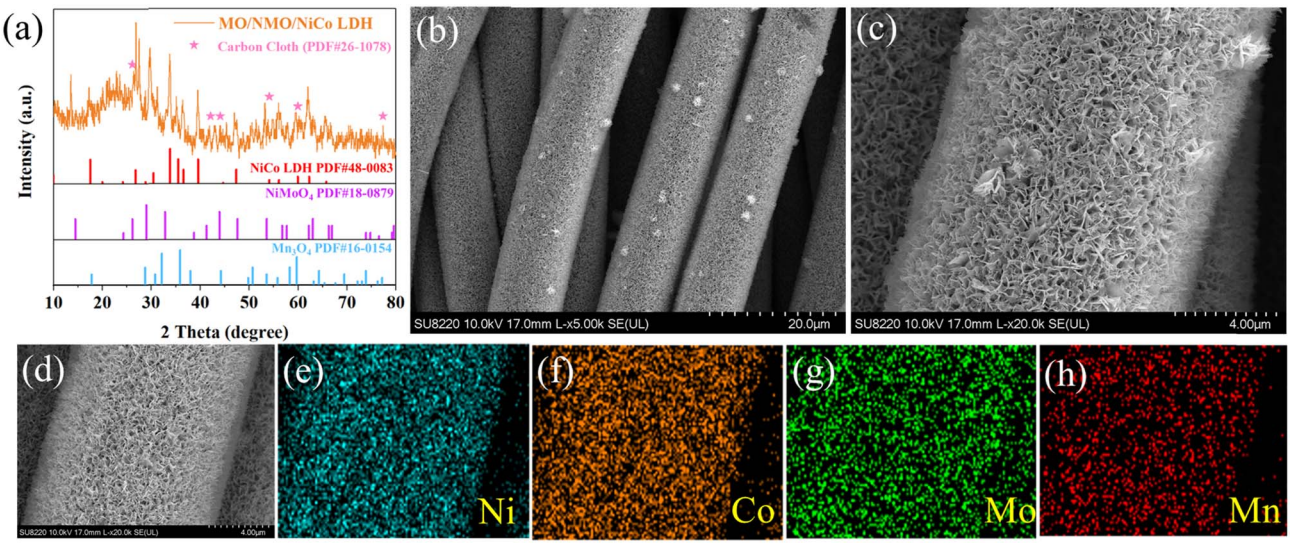

Fig. 1 (a) The XRD pattern of MO/NMO/NiCo LDH. (b and c) SEM images of MO/NMO/NiCo LDH. (d–h) Element mapping images corresponding to the SEM.

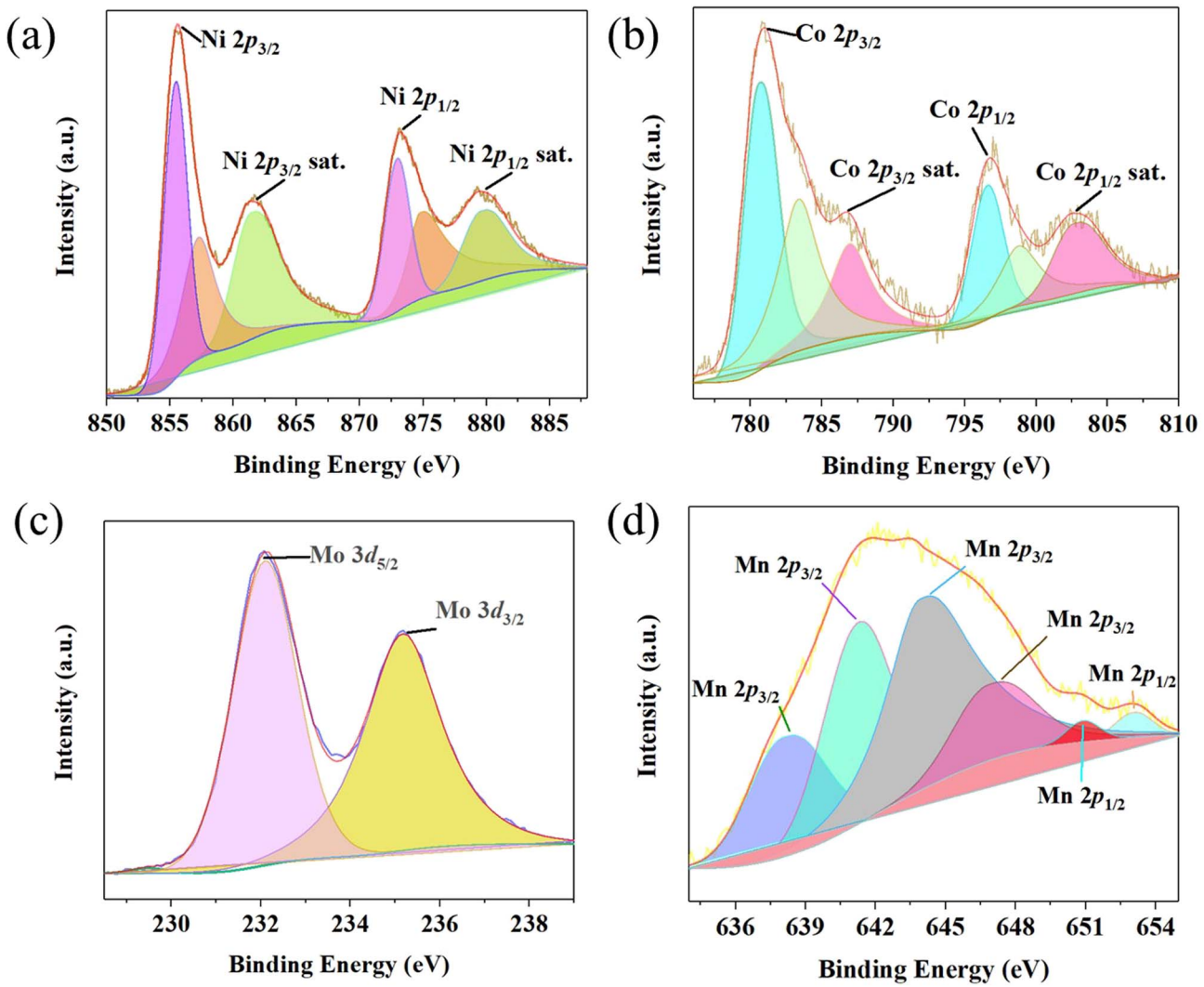

Fig. 2 XPS spectra of (a) Ni 2p, (b) Co 2p, (c) Mo 3d, and (d) Mn 2p.

synthesized samples. Due to the energy storage advantages of composite materials and porous structure, the MO/NMO/NiCo LDH positive electrode displays a high specific capacitance of 815 F g^{-1}, which is much larger than those of MO/NMO (525 F g^{-1}) and MO/NiCo LDH (135 F g^{-1}). As shown in Fig. 3c, all electrochemical impedance spectroscopy (EIS) curves consist of a quasi-semicircle (representing the charge transfer resistance (R_{ct}) caused by redox reaction) and an oblique line (revealing the

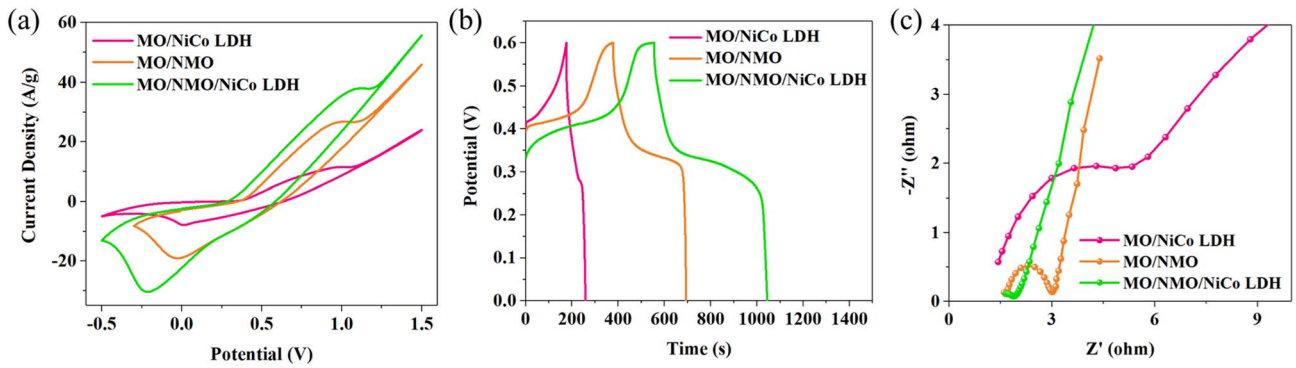

Fig. 3 The curves of MO/NMO/NiCo LDH, MO/NMO/NiCo LDH, and MO/NMO/NiCo LDH: (a) the CV curve at 30 mV s^{-1}, (b) GCD curve at 1 A g^{-1}, and (c) EIS curve.

diffusion behavior of ions).[14,15] The EIS curve of MO/NMO/NiCo LDH displays a smaller diameter semicircle and a larger slope in the linear part, which means that MO/NMO/NiCo LDH possesses a smaller R_{ct} and faster ion-diffusion rate than the other samples.

Recently, mass loading has been an important parameter to evaluate the application potential of an active material in a high capacity supercapacitor. Synthesizing an active material with high mass loading is still a promising strategy to improve high performance energy storage devices, though high mass loading leads to a sacrifice in electrochemical performance. Therefore, we investigated the electrochemical properties of MO/NMO/NiCo LDH with different mass loadings. It can be easily seen in Fig. S2† that the CV curve area and discharge time increase with the mass loading. In other words, the electrochemical performance of MO/NMO/NiCo LDH is enhanced instead of sacrificed with a high mass loading of 20.4 mg cm^{-2}. This reveals that MO/NMO/NiCo LDH has great application potential in high-capacity supercapacitors. Table 1 shows the specific capacitances and mass loadings of reported electrode materials. Compared to the reported materials,[16–20] the MO/NMO/NiCo LDH electrode in our work exhibited higher specific capacitance and higher mass loading. However, MO/NMO/NiCo LDH and MO/NMO/NiCo LDH show worse specific capacitance, which may be due to the poor conductivity and low ion diffusion brought by high mass loading.

Fig. 4a shows the CV curves of MO/NMO/NiCo LDH at different scan rates with the mass loading of 20.4 mg cm^{-2}. When the scan rate reaches 100 mV s^{-1}, both the oxidation peak and reduction peak are still visible, revealing the good energy storage behavior of MO/NMO/NiCo LDH. To confirm the pseudocapacitance behavior of MO/NMO/NiCo LDH, kinetic calculations were performed according to the CV curves. The relationship between the scan rate (v) and peak current (i) is described by the following formulas,[21]

$$i = av^b$$

$$\log i = b \log v + \log a$$

where both a and b are constants. The b value can be obtained from the slope of the log i–log v curve. As shown in Fig. 4b, the b values of the oxidation peak and reduction peak are 0.49908 and 0.53394, respectively, which are close to 0.5. This means that diffusion-controlled behavior accounts for the major proportion and the time of ions diffusing into the lattices is shortened.[22] The contribution ratio of capacitive and diffusion-controlled behavior was ascertained according to the following equation,[23]

$$i(v) = k_1 v + k_2 v^{1/2}$$

where i and v represent current and scan rate, respectively, $k_1 v$ is the contribution of capacitive processes and $k_2 v^{1/2}$ represents the contribution of diffusion-controlled processes. As can be seen in Fig. 4c, the contribution ratio of diffusion-controlled gradually decreases as the scan rate increases, which is caused by fast diffusion of ions into the material. Fig. 4d shows the GCD curves of MO/NMO/NiCo LDH at different current densities. The corresponding specific capacitances at each current density are 815 F g^{-1} (1 A g^{-1}), 703.33 F g^{-1} (2 A g^{-1}), 635 F g^{-1} (3 A g^{-1}), 541.67 F g^{-1} (5 A g^{-1}), 466.67 F g^{-1} (7 A g^{-1}), 316.67 F g^{-1} (10 A g^{-1}), and 193.33 F g^{-1} (20 A g^{-1}). In addition, the error bars of the specific capacitance are shown in Fig. S3.†

To reveal the application potential of high mass loading MO/NMO/NiCo LDH in a flexible supercapacitor, a FSC was assembled using MO/NMO/NiCo LDH as the anode, AC/CC as the cathode and polyvinyl alcohol (PVA)/KOH as the gel electrolyte in a sandwich structure, as shown in Fig. 5a. Fig. S4a† shows that the CV curve at 2.0 V displays no obvious polarization, which means the FSC can work stably at 2.0 V.[24] Fig. 5b shows the CV curves of the FSC at different scan rates from 10 mV s^{-1} to 200 mV s^{-1}. The redox peaks can be easily seen at the high scan rate of 200 mV s^{-1}, revealing the outstanding rate performance of the FSC. Fig. 5c shows the GCD curves of the FSC at different current densities and the corresponding specific capacitances of each GCD curve are 40.5 (1 A g^{-1}), 22.2 (2 A g^{-1}), 15.3 (3 A g^{-1}), 8 (5 A g^{-1}) and 3.5 F g^{-1} (7 A g^{-1}). Fig. 5d displays the relationship between the energy density and the power density of the FSC. The maximum energy density and power density of the FSC are 22.5 W h kg^{-1} and 8730 W kg^{-1}. It can be clearly seen that the FSC in this work possesses better performance than those of other reported supercapacitors, including the HPC-4//HPC-4 all-solid-state symmetric supercapacitor,[25] PANI@CNFs//PANI@CNFs flexible supercapacitor,[26] BIC-Co_3O_4//BIC-Co_3O_4 symmetric cell,[27] APC4/1//

Table 1 The specific capacitance and mass loading of the reported electrode materials

Electrode	Specific capacitance	Mass loading	Reference
Co–Ni LDH	811 F g^{-1}	3.59 mg cm^{-2}	16
Graphene films	340 F g^{-1}	4.8 mg cm^{-2}	17
Polyaniline-graphite	607 F g^{-1}	5.89 mg cm^{-2}	18
N-Doped porous carbon	457 F g^{-1}	1 mg cm^{-2}	19
Ni–Co–S	640 F g^{-1}	8.84 mg cm^{-2}	20
MO/NMO	525 F g^{-1}	15 mg cm^{-2}	This work
MO/NiCo LDH	135 F g^{-1}	13.8 mg cm^{-2}	This work
MO/NMO/NiCo LDH	815 F g^{-1}	20.4 mg cm^{-2}	This work

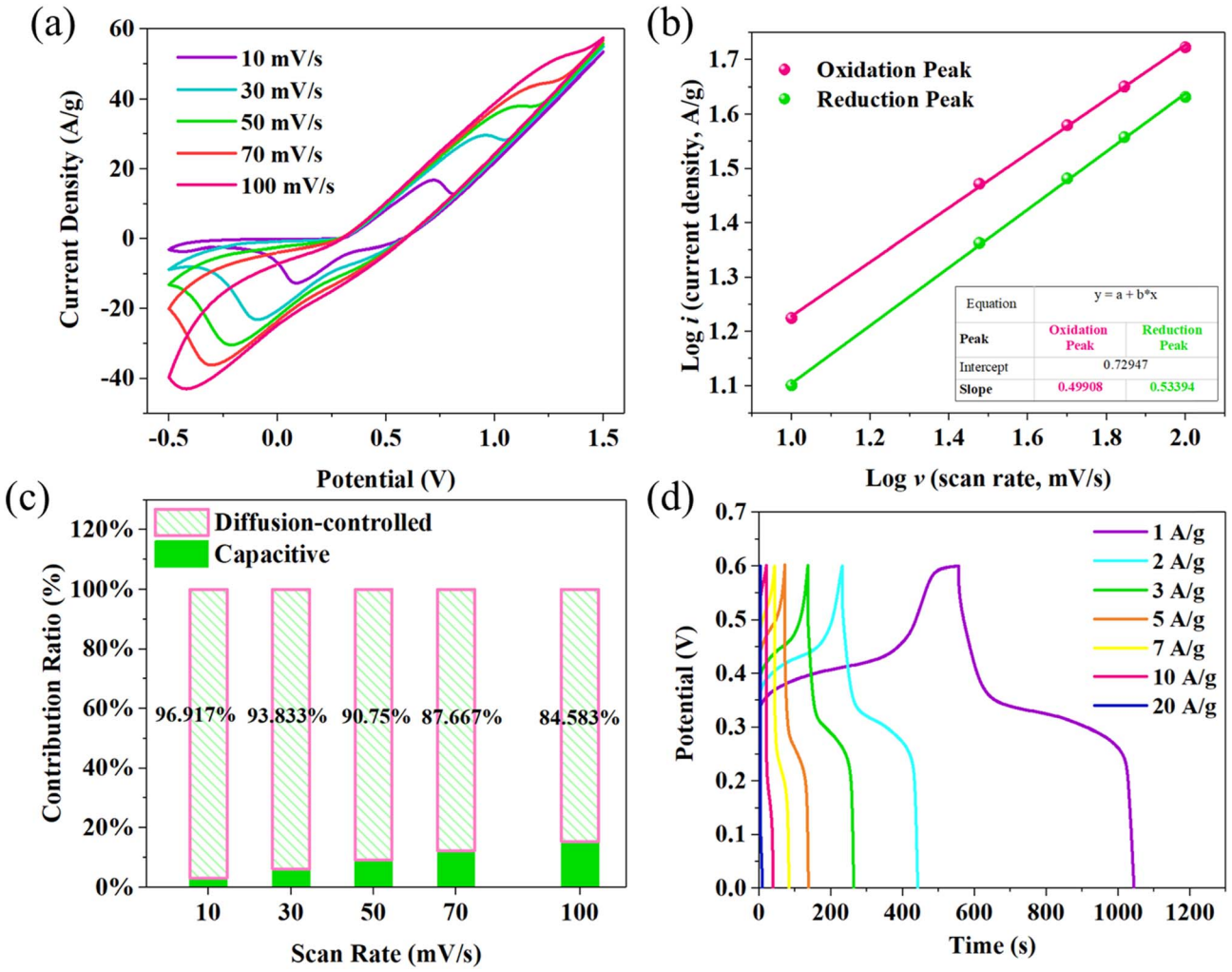

Fig. 4 (a) CV curves of MO/NMO/NiCo LDH at different scan rate. (b) The log i–log v curve, (c) contribution ratio between capacitive and diffusion-controlled, and (d) GCD curves of MO/NMO/NiCo LDH at different current densities.

APC4/1,[28] PANI/GF//PANI/GF device,[29] Ni_{33}/ZIF-67/rGO_{20}//Ni_{33}/ZIF-67/rGO_{20} all-solid-state supercapacitor[30] and L-$Ti_3C_2T_x$/E-ANF based flexible supercapacitor.[31]

Whether the FSC can work normally after deformation is an important indicator to measure its application potential in flexible devices. Fig. 5e shows the CV curves under different bending conditions. The CV curves under bending conditions show little difference and are obviously smaller in curve area than that of the original status. The corresponding area data of each curve are shown in Table S1.† The decrease in the CV curve area means that the performance of the FSC weakens during folding. This can be further proved by the GCD test. Fig. S4b† shows that the GCD curves under bending addition show little difference in shape to the original, which means that the FSC can work stably under bending conditions. In addition, the discharging time of each status is 81.2 s (original status, 40.5 F g^{-1}), 56.6 s (folded 200 times, 28.3 F g^{-1}), 54 s (folded 300 times, 27 F g^{-1}), 52.4 s (folded 400 times, 26.2 F g^{-1}), 50.2 s (folded 500 times, 25.1 F g^{-1}) and 49.4 s (folded 600 times, 24.7 F g^{-1}). In another words, the FSC kept 60.84% of the original specific capacitance after bending 600 times. The reduction of the CV curve area and discharging time may be attributed to the exfoliation of active material from the substrate. It is clearly shown in Fig. S4c† that the EIS curves under bending conditions possess smaller slopes than the original. To simulate the scenario of practical application, the long-term cycle performances of the FSC are evaluated at 5 A g^{-1}, and Fig. 5f shows the relationship between capacitance retention and cycles. The FSC possessed a high capacitance retention of 184.62% after 8000 GCD cycles and also retained 76.92% of the original specific capacitance after 15 000 cycles. The superior capacitance retention is due to the special structure of MO/NMO/NiCo LDH. During the high-current charge/discharge process, the 3D porous nanostructures of MO/NMO/NiCo LDH provide a large number of transport channels for electrons/ions as well as reactive active sites, which ensure the smooth progress of the redox reaction. Meanwhile, there is ample space for material expansion/contraction, greatly improving the cycle stability during long charge/discharge processes.

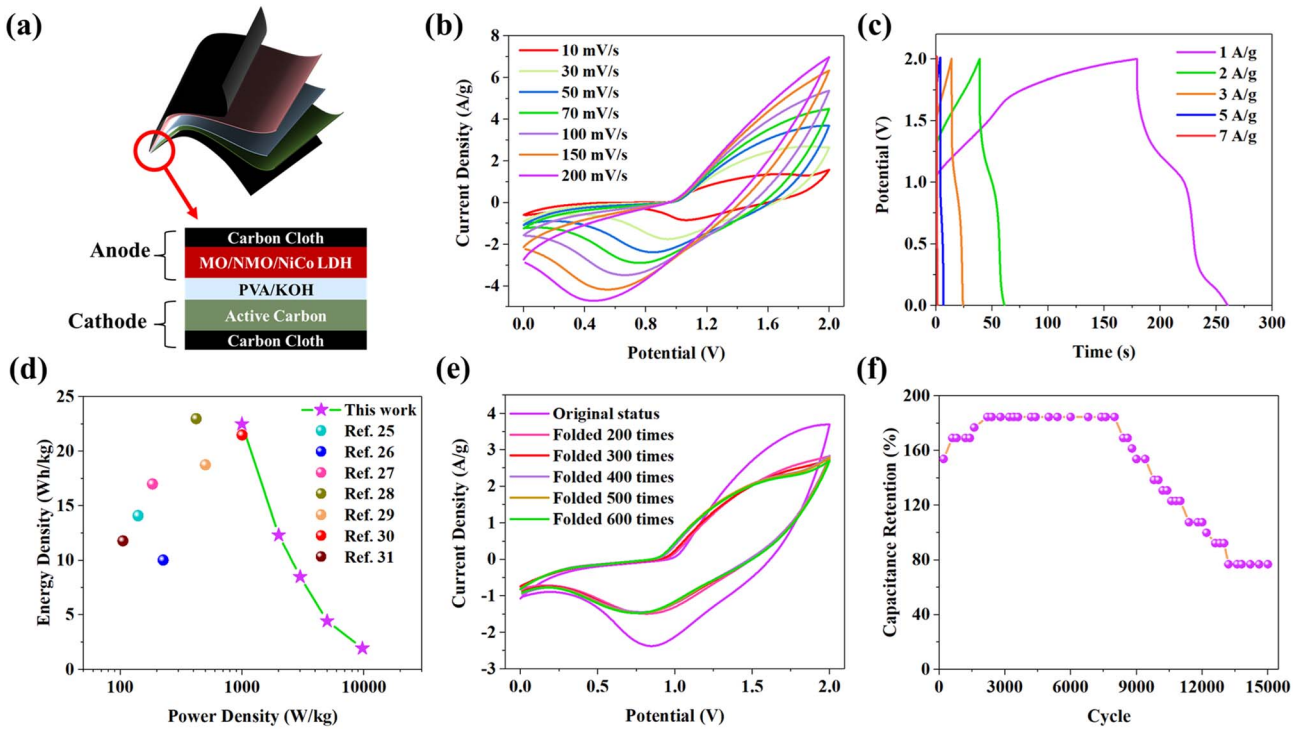

Fig. 5 (a) A diagram of the MO/NMO/NiCo LDH//AC FSC in a sandwich structure, (b) CV curves of the FSC at different scan rates, and (c) GCD curves of the FSC at different current densities. (d) The Ragone plot of the FSC, (e) CV curves of the FSC under different bending conditions, and (f) capacitance retention of the FSC during 15 000 GCD cycles.

3 Conclusion

The mass loading of electrode materials is a key parameter for their practical application in energy storage devices. Research on preparing electrode materials with high mass loading is the basis for developing high performance and high-capacity supercapacitors. In this work, the MO/NMO/NiCo LDH positive electrode with porous nanostructures and high loading (20.4 mg cm^{-2}) was successfully synthesized by electrodeposition on carbon cloth followed by hydrothermal method. The specific porous nanostructures of MO/NMO/NiCo LDH provided numerous ion/electron transport channels for redox reaction processing, enhancing the electrochemical performance. The MO/NMO/NiCo LDH positive electrode possessed good specific capacitance (815 F g^{-1} at 1 A g^{-1}) and good rate performance (redox peaks visible at 100 mV s^{-1}). The maximum energy density and power density of the MO/NMO/NiCo LDH//AC FSC were 22.5 W h kg^{-1} and 8730 W kg^{-1}. The FSC retained 60.84% of its original specific capacitance after bending to 180° 600 times. In addition, it kept 76.92% of its original specific capacitance after 15 000 GCD cycles. These results show that the MO/NMO/NiCo LDH positive electrode has great potential in application in high mass loading flexible supercapacitors, as it meets the development and needs of flexible devices. We believe this work can give some guidance in the preparation of high loading and high-capacity flexible supercapacitors.

4 Experimental details

4.1 Reagent

Urea (99%, AR) and KOH (90%, AR) were acquired from Shanghai trial. $NiCl_2 \cdot 6H_2O$ (99%, AR), $CoCl_2 \cdot 6H_2O$ (99%, AR), $MnCl_2 \cdot 4H_2O$ (99.99%, metals basis) and NaCl (99%, metals basis) were bought from Macklin. PVA ($M_w \sim 145\,000$) and $(NH_4)_6Mo_7O_{24}$ ($M_w \sim 1235.86$) were from Aladdin.

4.2 Synthesis of MO on CC

A piece of CC (1 cm × 2 cm) was cleaned with deionized water and absolute ethyl alcohol under ultrasonic processing for 30 min. Then, the CC was dried at 60 °C for 12 h.

The electrochemical growth of MO was processed by the cyclic voltammetry (CV) method, modified from Raut's work.[10] 5 mM $MnCl_2 \cdot 4H_2O$ and 5 mM NaCl were dissolved in 50 mL deionized water to prepare the precursor solution. The electrodeposition was performed in a three-electrode system, with the CC as the working electrode with a soak area of 1 cm × 1 cm, a platinum plate as the counter electrode, and a saturated calomel electrode as the reference electrode. The CV process was performed in the potential window of 0–1 V at 10 mV s^{-1} for 4 cycles. After the deposition, the electrodeposited MO was cleaned and dried for 6 h. The mass of MO deposited on the CC was 7.4 mg.

4.3 Preparation of NMO on MO

1 mM $NiCl_2 \cdot 6H_2O$ and 0.2 mM $(NH_4)_6Mo_7O_{24}$ were dissolved into 30 mL deionized water and transferred into a 100 mL

Teflon autoclave with the MO immersed. The solution was heated at 150 °C for 10 h. The sample (MO/NMO) was cleaned and dried at 60 °C for 12 h. The mass of the NMO on MO was 7.6 mg.

4.4 Synthesis of MO/NMO/NiCo LDH

1 mM $NiCl_2 \cdot 6H_2O$, 2 mM $CoCl_2 \cdot 6H_2O$ and 7 mM urea were dissolved into 30 mL deionized water. The obtained solution with MO/NMO immersed was heated at 120 °C for 10 h. The MO/NMO/NiCo LDH was cleaned and dried at 60 °C for 12 h. The NiCo LDH synthesized on MO/NMO was 5.4 mg.

The total mass of MO/NMO/NiCo LDH was 20.4 mg cm^{-2}. In addition, for comparison, MO/NMO and MO/NiCo LDH were synthesized by the same process.

4.5 Assembled supercapacitor

The MO/NMO/NiCo LDH//AC FSC was assembled using MO/NMO/NiCo LDH as the anode, AC as the cathode and PVA/KOH as the gel electrolyte. PVA/KOH was prepared by adding 3 g PVA to 30 mL of deionized water and stirring at 85 °C until the solution became clear. 10 mL of 3 M KOH was added into the solution under stirring and PVA/KOH was obtained.

4.6 Characterization methods

The X-ray diffraction patterns (XRD, Smartlab 9 kW) were detected in the Bragg's angle (2θ) range of 10–80° by Cu Kα radiation. X-ray photoelectron spectroscopy (XPS, Nexsa) was performed to verify the chemical states of the prepared samples. Field-emission scanning electron microscopy (FESEM, Hitachi, SU8010) was utilized to obtain the morphology.

4.7 Electrochemical measurement

The electrochemical performance was studied by performing CV, galvanostatic charge–discharge (GCD), and electrochemical impedance spectroscopy (EIS) on a IVIUM electrochemical workstation. The three-electrode system consisted of the synthesized electrode as the working electrode, HgO/Hg as the reference electrode and platinum plate as the counter electrode in 3 M KOH solution.

Conflicts of interest

The authors declare no competing financial interest.

Acknowledgements

This work was supported by Guangdong Science and Technology Plan (No. 2022A0505020022), Research Fund of Guangdong-Hong Kong-Macao Joint Laboratory for Intelligent Micro-Nano Optoelectronic Technology (No. 2020B1212030010), Guangdong Provincial Key Laboratory of Semiconductor Micro Display (2020B121202003) and Youth project of Guangdong Foshan joint fund of Guangdong Natural Science Foundation (Grant No. 2020A1515110601).

References

1 H. J. Zhou, G. Y. Zhu, S. Y. Dong, P. Liu, Y. Y. Lu, Z. Zhou, S. Cao, Y. Z. Zhang and H. Pang, *Adv. Mater.*, 2023, **35**, 2211523.
2 C. L. Liu, Y. Bai, W. T. Li, F. Y. Yang, G. X. Zhang and H. Pang, *Angew. Chem., Int. Ed.*, 2022, **61**, e202116282.
3 X. F. Zhang, X. D. Liu, R. Z. Yan, J. Q. Yang, Y. Liu and S. L. Dong, *J. Mater. Chem. C*, 2020, **8**, 2008–2013.
4 A. Barua, P. Mehra and A. Paul, *ACS Appl. Energy Mater.*, 2021, **4**, 14249–14259.
5 H. Ashassi-Sorkhabi and P. La'le Badakhshan, *Appl. Surf. Sci.*, 2017, **419**, 165–176.
6 Y. M. He, W. J. Chen, X. D. Li, Z. X. Zhang, J. C. Fu, C. H. Zhao and E. Q. Xie, *ACS Nano*, 2013, **7**, 174–182.
7 Z. H. Huang, Y. Song, D. Y. Feng, Z. Sun, X. Q. Sun and X.-X. Liu, *ACS Nano*, 2018, **12**, 3557–3567.
8 D. J. Wu, S. H. Xu, C. Zhang, Y. P. Zhu, D. Y. Xiong, R. Huang, R. J. Qi, L. W. Wang and P. K. Chu, *J. Mater. Chem. A*, 2016, **4**, 11317–11329.
9 L. Chen, F. Wang, Z. W. Tian, H. T. Guo, C. Y. Cai, Q. J. Wu, H. J. Du, K. M. Liu, Z. F. Hao, S. J. He, G. G. Duan and S. H. Jiang, *Small*, 2022, **18**, 2201307.
10 L. Wan, J. X. Liu J, Y. Zhang, J. Chen, C. Du and M. J. Xie, *Int. J. Hydrogen Energy*, 2020, **45**, 4521–4533.
11 X. Feng, J. Ning, D. Wang, J. C. Zhang, M. Y. Xia, Y. Wang and Y. Hao, *J. Alloys Compd.*, 2020, **816**, 152625.
12 R. B. Liang, Y. Q. Du, J. X. Wu, X. T. Li, T. X. Liang, J. Yuan, P. Xiao and J. W. Chen, *J. Solid State Chem.*, 2022, **307**, 122845.
13 R. B. Liang, Y. Q. Du, J. R. Lin, J. W. Chen and P. Xiao, *Energy Fuels*, 2022, **26**, 7115–7120.
14 J. Z. Ji, X. X. Pan, J. H. Qin, X. M. Chen and Q. B. Zha, *J. Electron. Mater.*, 2020, **49**, 4010–4017.
15 L. L. Jiang, X. T. Mei, D. L. Gan, S. W. Song, X. B. Lei, F. G. Cai, Y. Q. Wang, Q. Y. Zhang, X. Lu and Z. F. Ren, *Chem. –Eur. J.*, 2021, **27**, 5761–5768.
16 H. X. Wang, H. Yang, D. Wang, D. Y. Cheng, T. Deng, H. Y. Liu, H. B. Zhang, W. Zhang and W. T. Zheng, *Nanotechnology*, 2020, **31**, 105402.
17 Y. Zhao, J. Z. Liu, D. Z. Zheng, B. Wang, M. J. Hu, J. B. Sha and Y. Li, *Small*, 2018, **14**, 1702809.
18 Y. J. Ye, Z. H. Huang, Y. Song, J. W. Geng, X. X. Xu and X. X. Liu, *Electrochim. Acta*, 2017, **240**, 72–79.
19 L. Z. Sheng, Y. Y. Zhao, B. Q. Hou, Z. P. Xiao, L. L. Jiang and Z. J. Fan, *N. Carbon Mater.*, 2021, **36**, 167–175.
20 Y. X. Wen, Y. P. Liu and D. Y. He, *ACS Appl. Energy Mater.*, 2021, **4**, 6531–6541.
21 H. Liu, H. Guo, W. Q. Yao, L. W. Zhang, M. Y. Wang, T. Fan, W. H. Yang and W. Yang, *Colloids Surf., A*, 2020, **601**, 125011.
22 W. Lu, Z. Yuan, C. Y. Xu, J. Q. Ning, Y. J. Zhong, Z. Y. Zhang and Y. Hu, *J. Mater. Chem. A*, 2019, **7**, 5333–5343.
23 J. Wang, J. Polleux, J. Lim and B. Dunn, *J. Phys. Chem. C*, 2007, **111**, 14925–14931.
24 Y. Yue, Y. L. Huang and S. W. Bian, *ACS Appl. Electron. Mater.*, 2021, **3**, 2178–2186.

25 G. Z. Zhao, Y. J. Li, G. Zhu, J. Y. Zhu, T. Lu and L. K. Pan, *Ionics*, 2019, **25**, 3935–3944.
26 C. L. Hu, X. Y. Zhang, B. Liu, S. Y. Chen, X. Q. Liu, Y. M. Liu, J. Y. Liu and J. Chen, *Electrochim. Acta*, 2020, **338**, 135846.
27 K. J. Samdani, S. H. Kim, J. H. Park, S. H. Hong and K. T. Lee, *J. Ind. Eng. Chem.*, 2019, **74**, 96–102.
28 M. L. Wang, T. Y. Zhang, M. Z. Cui, W. F. Liu, X. G. Liu, J. W. Zhao and J. D. Zhou, *Chin. Chem. Lett.*, 2021, **32**, 1111–1116.
29 B. Liu, X. Y. Zhang, D. Tian, Q. Li, M. Zhong, S. Y. Chen, C. L. Hu and H. B. Ji, *ACS Omega*, 2020, **5**, 32395–32402.
30 S. Sundriyal, V. Shrivastav and S. Mishra S, *Int. J. Hydrogen Energy*, 2020, **45**, 30859–30869.
31 X. M. Yang, T. Li, X. X. He, Q. Li, J. Sun, Z. B. Lei and Z. H. Liu, *J. Power Sources*, 2022, **520**, 230899.